Heavy *d*-electron quasiparticle interference and real-space electronic structure of $Sr_3Ru_2O_7$

Jinho Lee[1,2,3]★, M. P. Allan[1,2]★, M. A. Wang[2], J. Farrell[1], S. A. Grigera[1,4], F. Baumberger[1], J. C. Davis[1,2,3] and A. P. Mackenzie[1†]

The intriguing idea that strongly interacting electrons can generate spatially inhomogeneous electronic liquid-crystalline phases is over a decade old[1–5], but these systems still represent an unexplored frontier of condensed-matter physics. One reason is that visualization of the many-body quantum states generated by the strong interactions, and of the resulting electronic phases, has not been achieved. Soft condensed-matter physics was transformed by microscopies that enabled imaging of real-space structures and patterns. A candidate technique for obtaining equivalent data in the purely electronic systems is spectroscopic imaging scanning tunnelling microscopy (SI-STM). The core challenge is to detect the tenuous but 'heavy' momentum (k)-space components of the many-body electronic state simultaneously with its real-space constituents. $Sr_3Ru_2O_7$ provides a particularly exciting opportunity to address these issues. It possesses a very strongly renormalized 'heavy' *d*-electron Fermi liquid[6,7] and exhibits a field-induced transition to an electronic liquid-crystalline phase[8,9]. Finally, as a layered compound, it can be cleaved to present an excellent surface for SI-STM.

The electronic structure of $Sr_3Ru_2O_7$ is complicated owing to both its bilayer nature and the in-plane $\sqrt{2} \times \sqrt{2}$ crystalline reconstruction caused by rotations of the RuO_6 octahedra (Fig. 1, inset). Nevertheless, photoemission studies reveal at least five Fermi-surface pockets[6], in agreement with de Haas–van Alphen data[7]. The most striking result of these **k**-space spectroscopic measurements is that the intense electron–electron interactions cause bands that are 10–30 times flatter than they would be if quasi-free electrons existed in the system. Thus, although its metallic state is a Fermi liquid, $Sr_3Ru_2O_7$ is one of the most strongly renormalized heavy *d*-electron compounds known, and consequently, the spectral weight of **k**-space excitations should be markedly reduced. This system undergoes a series of metamagnetic transitions in fields between 7.5 and 8.1 T applied parallel to the crystallographic *c* axis. These transitions enclose an H–T plane region within which a large resistivity enhancement occurs[8]. Application of further in-plane fields produces an 'easy' transport direction for which this enhanced resistivity disappears[10]. Thus, electronic transport with 180° rotational (C_2) symmetry exists within this narrow H–T region, whereas the surrounding regions exhibit transport with the expected 90° rotational (C_4) symmetry. These are the transport characteristics expected of a field-induced electronic nematic[10]—in this case, one generated from a many-body state of Ru *d*-electrons comprising both **r**-space and **k**-space spectral contributions.

SI-STM is potentially an ideal technique for studying such systems because simultaneous studies of **r**-space and **k**-space electronic structure can be carried out. It was pioneered in studies of simple quasi-free-electron systems[11,12] but, at least conceptually, might provide a route for imaging the far more complex many-body states of strongly correlated heavy-fermion systems. In SI-STM, measurement of the STM tip–sample differential tunnelling conductance $dI/dV(\mathbf{r}, V) \equiv g(\mathbf{r}, E = eV)$ at locations **r** and sample-bias voltage V, yields an image proportional to the local density of electronic states $LDOS(\mathbf{r}, E)$. Moreover, **k**-space electronic structure elements can be determined simultaneously by using Fourier-transform scanning tunnelling spectroscopy (FT-STS). This is because the spatial modulations in $g(\mathbf{r}, V)$ due to interference of quasiparticles scattered by atomic-scale impurities are detectable in $g(\mathbf{q}, V)$, the Fourier transform of $g(\mathbf{r}, V)$. The **k**-space states undergoing the scattering interference have been deduced for both quasi-free electrons of noble metals[11,12] and the weakly renormalized electronic states of superconducting cuprates[13–18] in a process dubbed quasiparticle interference (QPI) imaging.

Multiple challenges exist in extending the basic techniques used for simple quasi-free electrons[11,12] to many-body states in a strongly correlated heavy-fermion system such as $Sr_3Ru_2O_7$. The larger the mass renormalization due to electron–electron interactions becomes, the less the one-electron spectral weight in the **k**-space quasiparticles. As SI-STM is a single-electron spectroscopy, this loss of spectral weight is potentially a severe problem for detectability of **k**-space states by scattering interference. Another challenge is the complexity of the band structure[6,19]. In the case of simple metals and the cuprates, the reasons for the success of QPI is the combination of simple, un-renormalized band structures and a large joint density of states (JDOS) to enhance the intensity of the experimental signal[11–15]. However, for multiple, topographically complex bands, one cannot assume that the equivalent process is even possible. Thus, detection of the heavy quasiparticles of a correlated many-body state using QPI seems extremely difficult, and, perhaps for this reason, it had not been attempted until now. Here, however, we are motivated by the possibility that if both the **r**-space and **k**-space electronic structure of $Sr_3Ru_2O_7$ can be imaged using techniques that may be applied in high magnetic fields, this would open the way for this material to become a 'hydrogen atom' for the study of the many-body states forming electronic liquid crystals.

To explore these issues, we have carried out a SI-STM study on single crystals of $Sr_3Ru_2O_7$. The necessary scattering centres are introduced by replacing Ru atoms with Ti. To maximize the signal-to-background ratio of QPI, we needed to

---

[1]Scottish Universities Physics Alliance, School of Physics and Astronomy, University of St Andrews, St Andrews, Fife KY16 9SS, Scotland, [2]LASSP, Department of Physics, Cornell University, Ithaca, New York 14853, USA, [3]CMP&MS Department, Brookhaven National Laboratory, Upton, New York 11973, USA, [4]Instituto de Fisica de Liquidos y Sistemas Biologicos, UNLP, La Plata 1900, Argentina. *These authors contributed equally to this work.
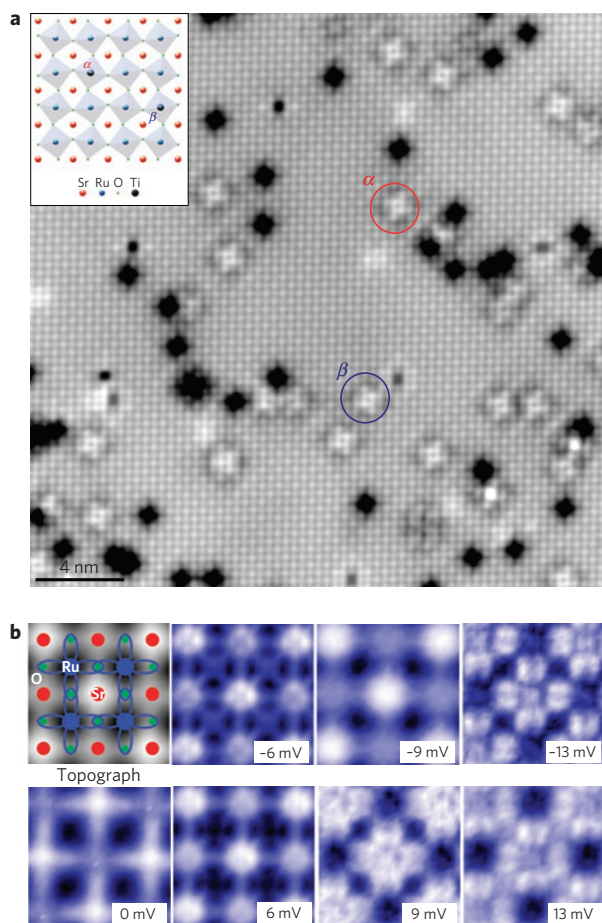[†]e-mail: apm9@st-andrews.ac.uk.

Figure 1 | Topography and sub-unit-cell electronic structure imaging in Sr₃Ru₂O₇. **a**, Topographic image of the SrO-cleaved $Sr_3Ru_2O_7$ surface, taken at −100 mV and 10 GΩ. The inset shows a schematic view from above along the c axis, showing the sequential 6.8° rotations of the RuO_6 octahedra, which double the unit-cell. The Ti dopant site is shown in black and two types of octahedron are labelled α and β. On the topographic image, dark and light spots stem from Ti impurities located at the Ru sites on the higher and lower RuO_2 sheet of the top bilayer, respectively. The white Ti sites appear in two different orientations, corresponding to the different RuO_6 octahedra orientations (inset). The data for Fig. 1b were taken far from any Ti dopant atom. **b**, The top left-hand panel shows the locations of Ru atoms and their d_{xz} and d_{yz} orbitals in blue. Red and green circles mark the positions of Sr, and O atoms, respectively. Each subsequent panel shows $g(\mathbf{r}, E)$ maps resolving sub-unit-cell spatial features in the same field of view. Whereas some $g(\mathbf{r}, E)$ show high intensity mainly at the positions of the Sr atoms (−9, 0 meV), others clearly resolve sub-unit-cell features with the symmetry and location of the d_{xz}, d_{yz} orbitals (−13, +9, +13 meV).

introduce a sufficient number of scattering centres to generate the interference patterns but sufficiently few not to significantly alter the electronic structure. Accordingly, we grew single crystals of $Sr_3(Ru_{0.99}Ti_{0.01})_2O_7$, that is, with 1% of the Ru atoms replaced by Ti.

Our samples are cooled in a cryogenic ultrahigh vacuum, cleaved between adjoining SrO planes, and inserted in the STM head at or below 4.2 K. Figure 1 shows a 28-nm-square topographic image of $Sr_3(Ru_{0.99}Ti_{0.01})_2O_7$. The quality of this image, and those previously obtained from $Sr_3Ru_2O_7$ (ref. 20), is related to a key advantage of Ruddlesden–Popper ruthenates for SI-STM studies of complex electronic matter. Each contains square planar Ru^{4+} coordinated with four oxygen atoms in a basic RuO_2 formula unit. This means that, unlike in the cuprates, all planes in

the material are charge-neutral, maximizing the possibility of obtaining cleaved surfaces that are bulk-representative. A top-view schematic diagram of the crystal structure is shown in the inset; it illustrates how Ti atoms substitute Ru in the RuO_2 plane and how the $\sqrt{2} \times \sqrt{2}$ reconstruction consists of sequential rotations of the RuO_6 octahedra about the c axis. In fact, the topographic data in Fig. 1 reveal all of these effects directly. Ti impurities from both upper and lower RuO layers are visible as dark and bright features respectively. The density of these features is in good agreement with the doped Ti density and they are absent in pure crystals. Moreover, the two different rotation angles corresponding to scattering from impurities in the two sublattices of each layer are also observable (labelled α and β for example in Fig. 1a).

Figure 1b shows the sub-unit-cell (see Supplementary Information) differential conductance mapping $g(\mathbf{r}, E)$ measurements of a typical $5 \times 5 \, Å^2$ field of view far from Ti impurities. Clear sub-atomic features are seen in the spatial arrangements of electronic structure, and there are several energies revealing **r**-space patterns expected of d_{xz}, d_{yz} orbitals. The type of atomic-resolution orbital occupancy imaging recently demonstrated in cuprates[21] may now become applicable to the Ru 4d states of $Sr_3Ru_2O_7$. The rate at which the **r**-space patterns evolve with energy is remarkable but could perhaps have been anticipated because, as we have emphasized, the electronic bands in $Sr_3Ru_2O_7$ are strongly renormalized by electron correlations[6,7]. In bands of mixed orbital character, the orbitals making the dominant contribution change as a function of **k** and energy. The images presented in Fig. 1b therefore probably represent the first real-space sub-atomic imaging of the energy evolution of strongly renormalized Wannier states; as such they invite more detailed theoretical investigation.

Fig. 2a–f shows a sequence of 28-nm-square $g(\mathbf{r}, E)$ images taken simultaneously and focused on the filled states. The most striking features are the strong $g(\mathbf{r}, E)$ oscillations near Ti atoms. Their dispersion is immediately obvious in the changes of $g(\mathbf{r}, E)$ in Fig. 2a–f. These changes occur because the LDOS$(\mathbf{r}, E)$ modulations exhibit characteristic wave vectors $\mathbf{q}(E)$ that disperse rapidly in energy. Figure 2g–l shows $g(\mathbf{q}, E)$, the Fourier-transformed images of Fig. 2a–f, respectively. The reciprocal-unit-cell locations of the Ru atoms are labelled as $(0, 2\pi/a_0)$; $(2\pi/a_0, 0)$ where a_0 is the shortest inter Ru distance. Raw $g(\mathbf{q}, E)$ are presented in Supplementary Fig. S1. The dispersions of the QPI patterns are manifest by the rapidly changing $g(\mathbf{q}, E)$, as is the complexity of scattering processes. These data reveal, for the first time, scattering interference of very heavy d-electron quasiparticles at individual impurity atoms.

To identify the bands responsible for these interferences, we consider the $Sr_3Ru_2O_7$ band structure[6,19] as outlined in Fig. 3a, where it would seem that numerous scattering **q**-vectors are possible. However, careful examination of the lengths, direction and dispersions of all of the observed $\mathbf{q}(E)$ in Fig. 2 directs our focus to the α_2 band, which has primarily $4d_{xz}, d_{yz}$ orbital character. Its $\mathbf{k}(E \sim E_f)$ contour is shown in comparison with the local-density-approximation band structure[6] in Fig. 3a, and throughout the larger unreconstructed Brillouin zone in Fig. 3b. The α_2-band spectral function $A(\mathbf{k}, E)$ is calculated from the $E(\mathbf{k})$ estimated from angle-resolved photoemission spectroscopy (ARPES; see Supplementary Information) and the resulting regions of high JDOS, which dominate the QPI processes[14,16,17] as estimated by taking the autocorrelation[22,23] of $A(\mathbf{k}, E)$ are shown in Fig. 3c. Overlaid are a sequence of inequivalent scattering vectors $\mathbf{q}_i : i = 1, \ldots, 10$ between the regions of high JDOS; these same vectors are shown in Fig. 3b to indicate how they interconnect the α_2 band. Remarkably, all of the inequivalent maxima in the complex $g(\mathbf{q}, E)$ between 5 meV and 13 meV below E_F can be accounted for using this model. This is shown, for example in Fig. 3d, by overlaying the positions of these same $\mathbf{q}_i$ on $g(\mathbf{q}, E = -9 \, \text{meV})$
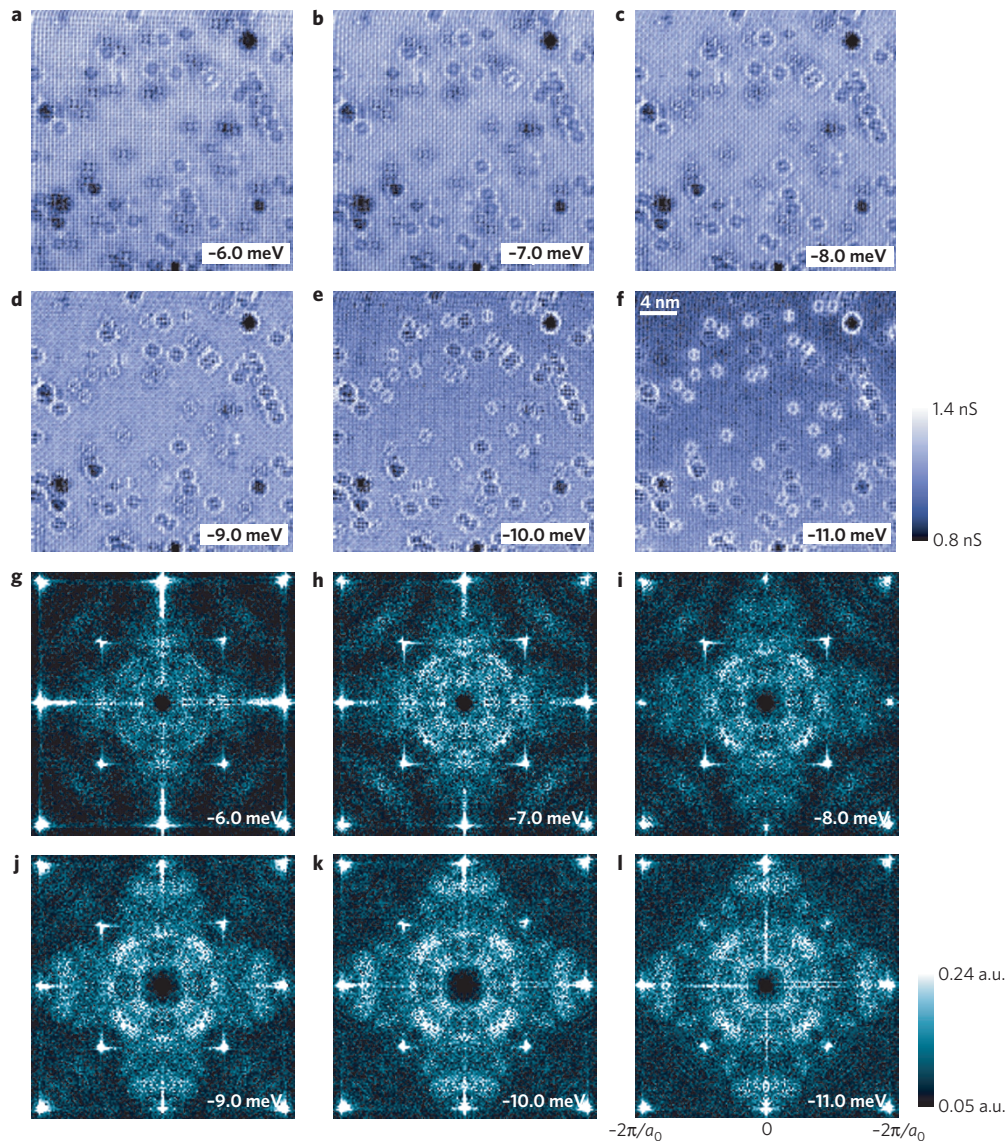
801

Figure 2 | FT-STS of $Sr_3Ru_2O_7$. a–f, A sequence of $g(\mathbf{r}, E)$ maps taken at -100 mV, $1\,G\Omega$ in the same 28-nm-square field of view. Each Ti scatterer exhibits energy-dispersive QPI fringes around it. **g–l**, The corresponding two-dimensional Fourier-transform image $g(\mathbf{q}, E)$, revealing heavy d-electron QPI directly. The dark area near $(0, 0)$ is where spectral weight has been reduced to allow for clearer viewing of the $g(\mathbf{q}, E)$ contrast and the images are octet-symmetrized (see Supplementary Information). A complex and fast-dispersing set of wave vectors $\mathbf{q}_i$ is seen in these $g(\mathbf{q}, E)$. Remarkably, this $\mathbf{q}$-space complexity and dispersion can be explained by scattering between states in only one very simple band of $Sr_3Ru_2O_7$.

from the model as open circles. The validity of the α_2 QPI model is then borne out by the good agreement and highly overdetermined internal consistency between the model in Fig. 3b and data in Fig. 3d. Moreover, when the dispersions of the two basic vectors $\mathbf{q}_1$ and $\mathbf{q}_2$ (Fig. 3b–d) are measured from Fig. 2g–l and plotted in Fig. 3e, they agree well with the directly measured dispersion of the α_2 band from ARPES (see Supplementary Information). In fact, dispersions of the $\mathbf{q}_i(E)$ (which will be described elsewhere) are also in good agreement with these conclusions. Thus, we find that the α_2 band is detectable directly by FT-STS in $Sr_3Ru_2O_7$ and that it dominates QPI at Ti atoms. The velocities identified from the dispersion in Fig. 3e are approximately $1 \times 10^4\,\mathrm{m\,s^{-1}}$, in good agreement with estimates based on ARPES and de Haas–van Alphen data[6,7]. These are ten times smaller than those seen in the α or β bands of Sr_2RuO_4, confirming the high mass and strong correlations of the quasiparticles in $Sr_3Ru_2O_7$. As to why the α_2 band should be predominant in QPI, one possibility is that strong momentum selective scattering effects due primarily to the correlations have a role[24].

These observations open the way for powerful modern SI-STM techniques[13–18] to be applied to many-body states not just in $Sr_3Ru_2O_7$, but also to a much wider class of strongly correlated heavy-fermion systems, including those that are spatially inhomogeneous. With regard to the problem of electronic nematicity in $Sr_3Ru_2O_7$, studies using the techniques introduced here but at high magnetic fields will be crucial. The current findings give at least two routes to microscopic investigation of a nematic state. First, the ability to resolve sub-atomic structure representative of the underlying orbitals offers the possibility of direct observation of lowered symmetry in their arrangement within the nematic region. Second, it is conceivable that the heavy d-electron QPI response will also show lowered symmetry. The density of Ti atoms chosen for the work reported here increases the residual resistivity of $Sr_3Ru_2O_7$ to $\sim$10 $\mu\Omega$ cm. This does not cause either an electronic or structural phase transition or a change to the Fermi energy, but would wash out the bulk signals of nematicity. However, the Ti level in the crystals can be controlled with high precision, and now
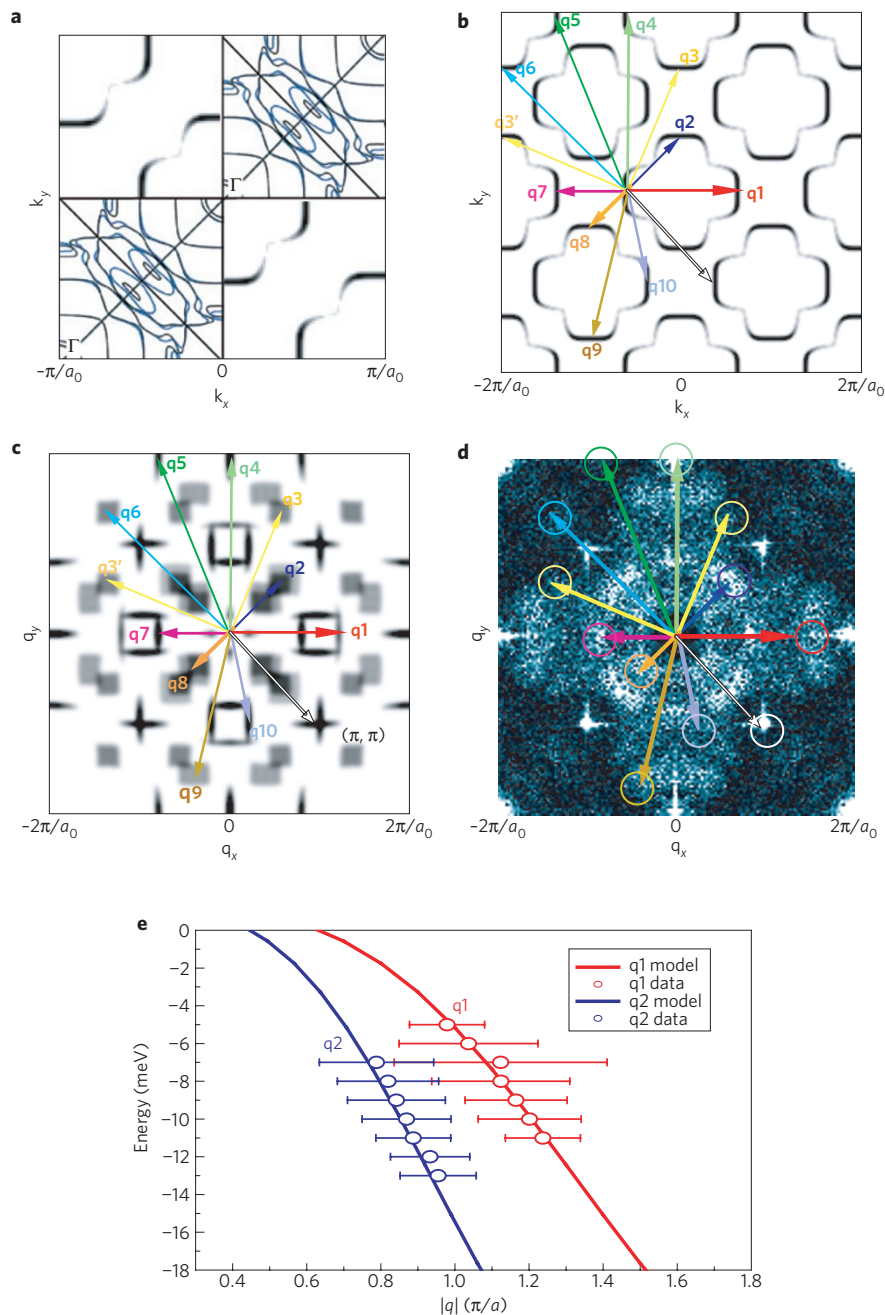
Figure 3 | Quasiparticle interference in the α_2 band of Sr$_3$Ru$_2$O$_7$. a, The local-density-approximation band structure in the first Brillouin zone (top right and bottom left quadrants) compared with the α_2 band of our model (top left and bottom right quadrants). **b**, The model $A(\mathbf{k},E)$ of the α_2 band in the extended zone scheme at $E = -9$ meV. The full set of inequivalent scattering vectors $\mathbf{q}_i : i = 1, \ldots, 10$ involving only the α_2 band is shown as coloured arrows (same arrows in **c,d**). This $A(\mathbf{k},E)$ is calculated from the α_2 band model estimated from ARPES measurements. **c**, The autocorrelation of the model α_2 shown in **b**. This process picks out the regions of high JDOS, which should dominate the quasiparticle scattering process. The full set of inequivalent scattering vectors $\mathbf{q}_i : i = 1, \ldots, 10$ that should exist for scattering interference only in the α_2 band is determined from these regions of high JDOS and is shown using the set of coloured arrows. **d**, By overlaying as open circles the tip positions of these same $\mathbf{q}_i$ on $g(\mathbf{q}, E = -9$ meV$)$, we see that all inequivalent maxima can be accounted for with highly overdetermined internal consistency by α_2 band scattering interference. **e**, Measured dispersions of $\mathbf{q}_1$ and $\mathbf{q}_2$ from data in Fig. 2g–l. They agree well with the model α_2 band, underlaid as the solid line, and thus with the directly measured dispersion of the α_2 band from ARPES (see Supplementary Information). The error bars indicate standard deviation widths of $\mathbf{q}_1$ and $\mathbf{q}_2$ peaks along the dispersion lines after fitting them to Gaussian curves at each energy.

that the basic characteristics of heavy d-electron QPI have been established, it will be possible to study samples with an order of magnitude fewer Ti inclusions.

The observations that the strongest QPI signals come from the α_2 band, and that $\mathbf{r}$-space structures associated with the same d_{xy}, d_{yz} orbitals are detectable, are both potentially important.

Early theoretical studies of the metamagnetism in Sr$_3$Ru$_2$O$_7$ focused on a proposed van Hove singularity and explained metamagnetism as being due to spin-splitting of its high density of states[25]. After the discovery of coexisting nematicity[10], a heuristic quadrupole electron–electron interaction connecting metamagnetism and nematicity was proposed[26]. More recent

theoretical advances propose spatially heterogeneous states caused by these singularities[27], or model the fundamental microscopic cause of metamagnetic nematicity in $Sr_3Ru_2O_7$ as being due to the natural uni-directionality of underlying d_{xz} d_{yz} orbitals and the related quasi-one-dimensional van Hove singularity[28,29]. Thus, in addition to our results having broad significance to the study of strongly renormalized metals, both the **r**-space and **k**-space electronic structure we report here may have relevance to the formation of an intriguing electronic liquid-crystal phase.

Methods

Crystal growth. The crystals used for this work were grown in St Andrews in a NEC Machinery Corporation Image furnace (SCI-MDH-11020). Batches of $Sr_3(Ru_{1-x}Ti_x)_2O_7$ were prepared by mixing RuO_2, TiO_2 and dried $SrCO_3$ powders in the ratio $2.52(1 - x):2x:3$. The mixed powder was then reacted in air at $1200\,^\circ C$ for 12 h, reground, formed into a feed-rod and sintered on a layer of strontium ruthenate bedding powder for 2 h at $1420\,^\circ C$, again in air. The rod was then melted in the image furnace, with crystalline growth seeded from the molten zone using a ruthenate seed crystal, and the polycrystalline rod fed into the molten zone at $25\,mm\,h^{-1}$. Gross phase purity was established using X-ray diffraction of powdered segments of the resultant single crystals and electron probe microanalysis was used to determine the Ti concentration. The residual resistivity was measured using standard four-probe techniques and an a.c. method. Typical currents were $100\,\mu A$ and frequencies were in the range 50–100 Hz. Data were taken in three cryostats: a continuous flow ^{4}He cryostat with a base temperature of 3.8 K, an adiabatic demagnetization refrigerator (Cambridge Magnetic Refrigeration) with a base temperature of 100 mK and a ^{3}He–^{4}He dilution refrigerator (Oxford Instruments) with a base temperature of approximately 30 mK.

Magnetic characterization was used to measure and then minimize the levels of $SrRuO_3$, Sr_2RuO_4 and $Sr_4Ru_3O_{10}$ impurity phases, which are always a challenge when growing this member of the Ruddlesden–Popper series of layered perovskite ruthenates. Sr_2RuO_4 inclusions can be identified by studying the diamagnetic a.c. response on entering the superconducting state. For quantitative work, care must be taken to operate in the low-demagnetizing-factor configuration in which the a.c. field is applied parallel to the ab planes. $SrRuO_3$ and $Sr_4Ru_3O_{10}$ are ferromagnetic with different Curie temperatures, so d.c. magnetization measurements in a commercial superconducting quantum interference device magnetometer (Quantum Design MPMS) allow a sensitive determination of small impurity contents. Full details of the characterization procedures can be found in ref. 30.

FT-STS measurements. To obtain QPI in **q**-space, we calculate the absolute intensity of the two-dimensional fast Fourier transform of the conductivity map $g(\mathbf{r}, E)$. This shows an extremely bright spot in the centre due to long-wavelength fluctuations. To remove these very small **q**-vector elements in q-space, we first subtract the data value averaged with a Gaussian filter width of about 6 Å from the original conductance value at every pixel. The two-dimensional Fourier transform of this resulting value effectively gets rid of the low-**q** vector components, showing clearer individual QPI features.

Owing to drift during a scan, the raw $g(\mathbf{r}, E)$ does not show perfect square symmetry, but is slightly elongated in one direction. To correct this effect, we use a conformal mapping algorithm to make $g(\mathbf{r}, E)$ a square. Here, we use information about the atomic Bragg peak positions to calculate the necessary parameters of the conformal transformation. Although the resulting Fourier-transform $g(\mathbf{q}, E)$ shows clear dispersive QPI features with fourfold symmetry, we attempted to enhance the signal-to-noise ratio even further. We selectively averaged symmetrical data points over two octants of $g(\mathbf{q}, E)$ showing more discernible intensity peaks which, in this study, happened to be along the vertical direction. Mathematically this operation corresponds to symmetrically averaging (averaging only among symmetrically equivalent points under fourfold symmetry) over the **q**-space region, which satisfies $|q_y| > |q_x|$, and using only this part to construct complete $g(\mathbf{q}, E)$.

References

1. Kivelson, S. A., Fradkin, E. & Emery, V. J. Electronic liquid-crystal phases of a doped Mott insulator. *Nature* **393,** 550–553 (1998).
2. Fradkin, E. & Kivelson, S. A. Liquid-crystal phases of quantum Hall systems. *Phys. Rev. B* **59,** 8065–8072 (1999).
3. Halboth, C. J. & Metzner, W. d-wave superconductivity and Pomeranchuk instability in the two-dimensional Hubbard model. *Phys. Rev. Lett.* **85,** 5162–5165 (2000).
4. Yamase, H. & Kohno, H. Instability toward formation of quasi-one-dimensional Fermi surface in two-dimensional t–J model. *J. Phys. Soc. Jpn* **69,** 2151–2157 (2000).
5. Zaanen, Z., Nussinov, Z. & Mukhin, S. I. Duality in 2+1D quantum elasticity: Superconductivity and quantum nematic order. *Ann. Phys.* **310,** 181–260 (2004).
6. Tamai, A. *et al.* Fermi surface and van Hove singularities in the itinerant metamagnet $Sr_3Ru_2O_7$. *Phys. Rev. Lett.* **101,** 026407 (2008).
7. Borzi, R. A. *et al.* de Haas–van Alphen effect across the metamagnetic transition in $Sr_3Ru_2O_7$. *Phys. Rev. Lett.* **92,** 216403 (2004).
8. Perry, R. S. *et al.* Multiple first-order metamagnetic transitions and quantum oscillations in ultrapure $Sr_3Ru_2O_7$. *Phys. Rev. Lett.* **92,** 166602 (2004).
9. Grigera, S. A. *et al.* Disorder-sensitive phase formation linked to metamagnetic quantum criticality. *Science* **306,** 1154–1157 (2004).
10. Borzi, R. A. *et al.* Formation of a nematic fluid at high fields in $Sr_3Ru_2O_7$. *Science* **315,** 214–217 (2007).
11. Crommie, M. F., Lutz, C. P. & Eigler, D. M. Imaging standing waves in a two-dimensional electron gas. *Nature* **363,** 524–527 (1993).
12. Petersen, L., Hofmann, Ph., Plummer, E. W. & Besenbacher, F. Fourier transform–STM: Determining the surface Fermi contour. *J. Electron Spectrosc. Relat. Phenom.* **109,** 97 (2000).
13. Hoffman, J. E. *et al.* Imaging quasiparticle interference in $Bi_2Sr_2CaCu2O_{8+d}$. *Science* **297,** 1148–1151 (2002).
14. Wang, Q.-H. & Lee, D.-H. Quasiparticle scattering interference in high-temperature superconductors. *Phys. Rev. B* **67,** 020511 (2003).
15. McElroy, K. *et al.* Relating atomic-scale electronic phenomena to wave-like quasiparticle states in superconducting $Bi_2Sr_2CaCu_2O_{8+\delta}$. *Nature* **422,** 592–596 (2003).
16. Capriotti, L., Scalapino, D. J. & Sedgewick, R. D. Wave-vector power spectrum of the local tunneling density of states: Ripples in a d-wave sea. *Phys. Rev. B* **68,** 014508 (2003).
17. Nunner, T. S., Chen, W., Andersen, B. M., Melikyan, A. & Hirschfeld, P. J. Fourier transform spectroscopy of d-wave quasiparticles in the presence of atomic scale pairing disorder. *Phys. Rev. B* **73,** 104511 (2006).
18. Hanaguri, T. *et al.* Quasiparticle interference and superconducting gap in $Ca_{2-x}Na_xCuO_2Cl_2$. *Nature Phys.* **3,** 865–871 (2007).
19. Singh, D. J. & Mazin, I. I. Electronic structure and magnetism of $Sr_3Ru_2O_7$. *Phys. Rev. B* **63,** 165101 (2001).
20. Iwaya, K. *et al.* Local tunneling spectroscopy across a metamagnetic critical point in the bilayer ruthenate $Sr_3Ru_2O_7$. *Phys. Rev. Lett.* **99,** 057208 (2007).
21. Kohsaka, Y. *et al.* An intrinsic bond-centered electronic glass with unidirectional domains in underdoped cuprates. *Science* **315,** 1380–1385 (2007).
22. McElroy, K. *et al.* Elastic scattering susceptibility of the high temperature superconductor $Bi_2Sr_2CaCu_2O_{8+x}$: A comparison between real and momentum space photoemission spectroscopies. *Phys. Rev. Lett.* **96,** 067005 (2006).
23. Chatterjee, U. *et al.* Nondispersive fermi arcs and the absence of charge ordering in the pseudogap phase of $Bi_2Sr_2CaCu_2O_{8+d}$. *Phys. Rev. Lett.* **96,** 107006 (2006).
24. Kim, E.-A. & Lawler, M. J. Interference of nematic quantum critical quasiparticles: A route to the octet model. Preprint at <http://arxiv.org/abs/0811.2242> (2009).
25. Binz, B. & Sigrist, M. Metamagnetism of itinerant electrons in multi-layer ruthenates. *Europhys. Lett.* **65,** 816–822 (2004).
26. Kee, H. Y. & Kim, Y. B. Itinerant metamagnetism induced by electronic nematic order. *Phys. Rev. B* **71,** 184402 (2005).
27. Berridge, A.M. *et al.* Inhomogeneous magnetic phases: A LOFF-like phase in $Sr_3Ru_2O_7$. *Phys. Rev. Lett.* **102,** 136404 (2009).
28. Raghu, S. *et al.* Microscopic theory of the nematic phase in $Sr_3Ru_2O_7$. *Phys. Rev. B* **79,** 214402 (2009).
29. Lee, W.C. & Wu, C. Nematic electron states enhanced by orbital band hybridization. Preprint at <http://arxiv.org/abs/0902.1337> (2009).
30. Farrell, J. E. *The Influence of Cation Doping on the Electronic Properties of $Sr_3Ru_2O_7$.* PhD thesis, Univ. St Andrews; available at <http://hdl.handle.net/10023/689>.

Author contributions

The crystals were grown by J.F., SI-STM experiments were carried out by J.L., M.P.A. and M.A.W. and project planning, data analysis and paper-writing were done by J.L., M.P.A., S.A.G., F.B., J.C.D. and A.P.M.

Additional information

Supplementary information accompanies this paper on www.nature.com/naturephysics. Reprints and permissions information is available online at http://npg.nature.com/reprintsandpermissions. Correspondence and requests for materials should be addressed to A.P.M.